

# Quantifying vegetation indices using Terrestrial Laser Scanning: methodological complexities and ecological insights from a Mediterranean forest

William Rupert Moore Flynn<sup>1</sup>, Harry Jon Foord Owen<sup>2</sup>, Stuart William David Grieve<sup>1,3</sup> and Emily Rebecca Lines<sup>2</sup>

<sup>1</sup>School of Geography, Queen Mary University of London, Mile End Rd, Bethnal Green, London E1 4NS

<sup>2</sup>Department of Geography, University of Cambridge, Downing Place, Cambridge, CB2 3EN

<sup>3</sup>Digital Environment Research Institute, Queen Mary University of London, New Road, London, E1 1HH

Correspondence to: W. R. M. Flynn ([w.r.m.flynn@qmul.ac.uk](mailto:w.r.m.flynn@qmul.ac.uk))

**Abstract.** Accurate measurement of vegetation density metrics including plant, wood and leaf area indices (PAI, WAI and LAI) is key to monitoring and modelling carbon storage and uptake in forests. Traditional passive sensor approaches, such as Digital Hemispherical Photography (DHP), cannot separate leaf and wood material, nor individual trees, and require many assumptions in processing. Terrestrial Laser Scanning (TLS) data offer new opportunities to improve understanding of tree and canopy structure. Multiple methods have been developed to derive PAI and LAI from TLS data, but there is little consensus on the best approach, nor are methods benchmarked as standard.

Using TLS data collected in 33 plots containing 2472 trees of five species in Mediterranean forests, we compare three TLS methods (*LiDAR Pulse*, *2D Intensity Image* and *Voxel-Based*) to derive PAI and compare with co-located DHP. We then separate leaf and wood in individual tree point clouds to calculate the ratio of wood to total plant area ( $\alpha$ ), a metric to correct for non-photosynthetic material in LAI estimates. We use individual tree TLS point clouds to estimate how  $\alpha$  varies with species, tree height and stand density.

We find the *LiDAR Pulse* method agrees most closely with DHP, but is limited to single scan data so cannot determine individual tree properties, including  $\alpha$ . The *Voxel-Based* method shows promise for ecological studies as it can be applied to individual tree point clouds. Using the *Voxel-Based* method, we show that species explain some variation in  $\alpha$ , however, height and plot density were better predictors.

Our findings highlight the value of TLS data to improve fundamental understanding of tree form and function, but also the importance of rigorous testing of TLS data processing methods at a time when new approaches are being rapidly developed. New algorithms need to be compared against traditional methods, and existing algorithms, using common reference data. Whilst promising, our results show that metrics derived from TLS data are not yet reliably calibrated and validated to the extent they are ready to replace traditional approaches for large scale monitoring of PAI and LAI.

## 33 **1 Introduction**

34 Terrestrial Laser Scanning (TLS) generates high-resolution 3D measurements of whole forests and individual  
35 trees (Burt et al., 2018; Disney, 2018), leading to the development of completely new monitoring approaches to  
36 understand the structure and function of ecosystems (Lines et al., 2022). Unlike traditional passive sensors, TLS  
37 can estimate plant, wood and leaf area indices (PAI; WAI; LAI) for both whole plots and individual tree point  
38 clouds (Calders et al., 2018), and is unaffected by illumination conditions. This has led to the development of  
39 several methods for processing TLS data to extract the key metrics PAI, WAI and LAI (e.g. Hosoi and Omasa,  
40 2006; Jupp et al., 2008; Zheng et al., 2013). However, intercomparison studies of algorithms and processing  
41 approaches to derive the same metrics from different TLS methods are lacking.

42 Leaf Area Index (LAI), defined as half the amount of green leaf area per unit ground area (Chen and Black, 1992),  
43 determines global evapotranspiration, phenological patterns and canopy photosynthesis, and is therefore an  
44 essential climate variable (ECV), as well as a key input in dynamic global vegetation models (Sea et al., 2011;  
45 Weiss et al., 2004). Accurate measurements of LAI, WAI and PAI have historically been derived from labour  
46 intensive destructive sampling (Baret et al., 2013; Jonckheere et al., 2004), so over large spatial or temporal scales  
47 these can only be measured indirectly, typically with remote sensing. Large-scale remote sensing, using  
48 spaceborne and airborne instruments, has been widely used to estimate LAI over large areas (Pfeifer et al., 2012),  
49 but requires calibration and validation using in situ measurements to constrain information retrieval (Calders et  
50 al., 2018). Non-destructive in situ vegetation index estimates have historically been made by measuring light  
51 transmission below the canopy and using simplifying assumptions about canopy structure to estimate the amount  
52 of intercepting material (e.g. Beer-Lambert law; Monsi and Saeki, 1953). The most common method, Digital  
53 Hemispherical Photography (DHP; Figure 1a), requires both model assumptions and subjective user choices  
54 during data acquisition and processing in order to estimate both PAI and LAI (Breda, 2003). DHP images are  
55 processed by separating sky from canopy, but not photosynthetic from non-photosynthetic vegetative material, so  
56 additional assumptions are needed to calculate either LAI or WAI (Jonckheere et al., 2004; Pfeifer et al., 2012).  
57 Separation of LAI from PAI can be achieved by removing or masking branches and stems from hemispherical  
58 images (e.g. Sea et al., 2011; Woodgate et al., 2016), but is not reliable when leaves are occluded by woody  
59 components (Hardwick et al., 2015). An alternative approach is to take separate DHP measurements in both leaf  
60 on and leaf off conditions, and derive empirical wood to plant ratios (WAI/PAI,  $\alpha$ ) (Leblanc and Chen, 2001), but  
61 this is not always practical, for example in evergreen forests. The difficulty of separation means that studies often  
62 omit correcting for the effect of WAI on optical PAI measurements altogether (Woodgate et al., 2016), but since  
63 woody components in the forest canopy can account for more than 30% of PAI (Ma et al., 2016) this can introduce  
64 overestimation. Further, although DHP estimates of LAI or PAI are valuable both for ecosystem monitoring and  
65 developing satellite LAI products (Hardwick et al., 2015; Pfeifer et al., 2012), they are limited to sampling only  
66 at a neighbourhood or plot level (Weiss et al., 2004), and cannot be used to measure individual tree LAI except  
67 for open grown trees (Béland et al., 2014).

68 The ratio of wood to total plant area,  $\alpha$ , is known to be dynamic, changing in response to abiotic and biotic  
69 conditions. For example, the Huber value (sapwood to leaf area ratio, a related measure to  $\alpha$ ) may vary according  
70 to water availability (Carter and White 2009). Leaf area may therefore be indicative of the drought tolerance level  
71 of a tree, with more drought tolerant species displaying a lower leaf area, reducing the hydraulic conductance of

72 the whole tree and therefore increasing its drought tolerance (Niinemets and Valladares, 2006).  $\alpha$  has been  
73 hypothesised to increase with the size of a tree in response to the increased hydraulic demand associated with  
74 greater hydraulic resistance of tall trees (Magnani et al., 2000) and higher transpiration rates of larger LAI  
75 (Battaglia et al., 1998; Phillips et al., 2003). Stand density may also impact  $\alpha$  (Long and Smith, 1988; Whitehead,  
76 1978), as increased stand level water use scales linearly with LAI (Battaglia et al., 1998; Specht and Specht, 1989),  
77 reducing water availability to individual trees competing for the same resources (Jump et al., 2017). Large scale  
78 quantification of  $\alpha$  or Huber value, however, is difficult as studies usually rely on a small number of destructively  
79 sampled trees (e.g. Carter and White, 2009; Magnani et al., 2000), litterfall traps (e.g. Phillips et al., 2003) or  
80 masking hemispherical images (e.g. Sea et al., 2011; Woodgate et al., 2016). These approaches are only applicable  
81 on a small to medium scale, and in the case of image masking, cannot differentiate between individuals. Variation  
82 in  $\alpha$ , for example by species and or stand structure, is therefore largely unknown.

### 83 **1.2 TLS methods for calculating PAI, LAI and WAI**

84 TLS methods for extracting PAI, LAI and WAI can be broadly categorised into two types: (1) LiDAR return  
85 counting, using single scan data (e.g., the *LiDAR Pulse* method; Jupp et al., 2008, and *2D Intensity Image* method;  
86 Zheng et al., 2013) and (2) point cloud voxelisation, usually using co-registered scans (e.g., the *Voxel-Based*  
87 method; Hosoi and Omasa, 2006).

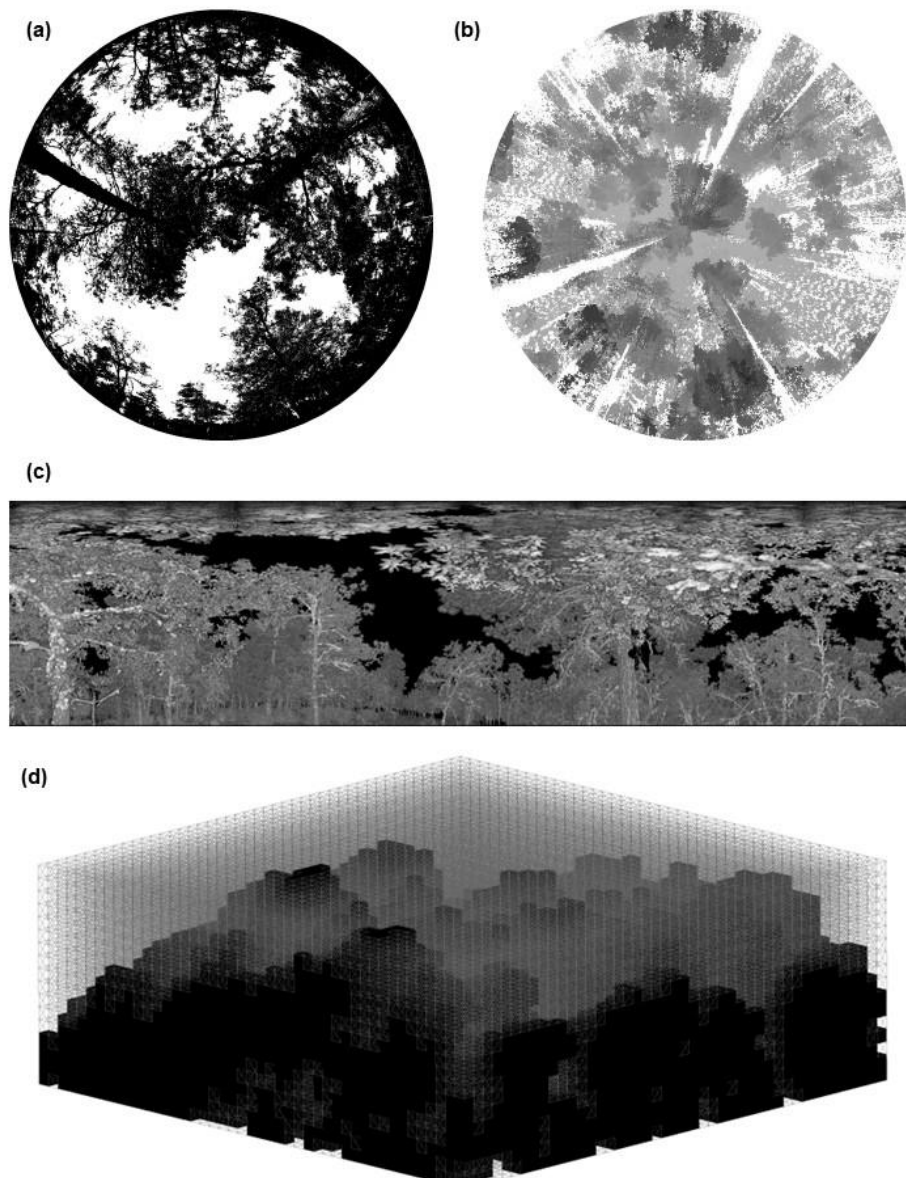
88 The *LiDAR Pulse* method (Jupp et al., 2008; Figure 1b) estimates gap fraction ( $P_{gap}$ ) using single scan data, as a  
89 function of the total number of outgoing LiDAR pulses from the sensor and the number of pulses that are  
90 intercepted by the canopy. This method, which eliminates illumination impacts associated with the use of DHP  
91 (Calders et al., 2014), has been implemented in the python module, *PyLidar* ([www.pylidar.org](http://www.pylidar.org)) and the R package,  
92 *rTLS* (Guzman, et al. 2021). Using the *LiDAR Pulse* method, Calderys et al. (2018) compared PAI estimates from  
93 two ground-based passive sensors (LiCOR LAI-2000 and DHP) with TLS data collected with a RIEGL VZ-400  
94 TLS in a deciduous woodland, and found the two passive sensors underestimated PAI values compared to TLS,  
95 with differences dependent on DHP processing and leaf on/off conditions.

96 The *2D Intensity Image* method (Zheng et al., 2013; Figure 1c), also uses raw single scan TLS point clouds, but,  
97 unlike the *LiDAR Pulse* method, converts LiDAR returns into 2D panoramas where pixel values represent return  
98 intensity. PAI is estimated by classifying pixels as sky or vegetation, based on their intensity value, to estimate  
99  $P_{gap}$ , and then applying Beer-Lambert's law. Like the *LiDAR Pulse* method, this approach has been shown to  
100 generate higher PAI estimates than DHP (Calderys et al., 2018; Woodgate et al., 2015; Grotti et al., 2020), with  
101 differences attributed to the greater pixel resolution and viewing distance of TLS resolving more small canopy  
102 details (Grotti et al., 2020).

103 The *Voxel-Based* method (Figure 1d) estimates PAI by segmenting a point cloud into voxels and either simulating  
104 radiative transfer within each cube (Béland et al., 2014; Kamoske et al., 2019), or classifying voxels as either  
105 containing vegetation or not, and dividing vegetation voxels by the total number of voxels (Hosoi and Omasa,  
106 2006; Itakura and Hosoi, 2019; Li et al., 2017). Crucially, this method may be applied to multiple co-registered  
107 scan point clouds and so can be used to calculate PAI for both whole plots and individual, segmented TLS trees.  
108 However, PAI estimates derived using the voxel method are highly dependent on voxel size (Calderys et al., 2020).  
109 Using a radiative transfer approach, Béland et al., (2014) demonstrated that voxel size is dependent on canopy

110 clumping, radiative transfer model assumptions and occlusion effects, making a single, fixed choice of voxel size  
111 for all ecosystem types, scanners or datasets impossible. To test various approaches to selecting voxel size using  
112 a voxel classification approach, Li et al., (2016) matched voxel size to point cloud resolution, individual tree leaf  
113 size, and minimum beam distance and tested against destructive samples, finding that voxel size matched to point  
114 cloud resolution had the closest PAI values to destructive samples.

115 The *LiDAR Pulse* method and *2D Intensity Image* method both use single scan data. However, to generate robust  
116 estimates of canopy properties that avoid errors from occlusion effects, multiple co-registered scans taken from  
117 different locations are likely needed (Wilkes et al., 2017). Further, both these methods require raw unfiltered data  
118 to accurately measure the ratio of pulses emitted from the scanner and number of pulses that are intercepted by  
119 vegetation. This means “noisy” points caused by backscattered pulses (Wilkes et al., 2017) are included in  
120 analyses, potentially leading to higher PAI estimates. However, the *LiDAR Pulse* and *2D Intensity Image* methods  
121 may introduce fewer estimation errors compared to DHP, which is influenced by differences in sky illumination  
122 conditions and camera exposure (Weiss et al., 2004).



124

125 **Figure 1: Visual representation of the four methods for PAI and WAI estimation used in this study: (a) a binarised**  
126 **digital hemispherical photograph (DHP), (b) TLS raw single scan point cloud, for the *LiDAR Pulse* method (Jupp et**  
127 **al., 2008). Image shows a top-down view of raw point cloud and greyscale represents low (grey) and high (black) Z**  
128 **values, (c) TLS 2D intensity image for the *2D Intensity Image* method (Zheng et al., 2013), (d) Voxelised co-registered**  
129 **whole plot point cloud for the *Voxel-Based* method (Hosoi and Omasa, 2006), showing a representative schematic of**  
130 **cube voxels with edge length of 1m, voxelised using the *R* package *VoxR* (Lecigne et al., 2018). Solid black voxels are**  
131 **classified as containing vegetation (filled) and voxels outlined with grey lines are voxels classified as empty.**

### 132 **1.3 Scope and aims**

133 The aims of this study are twofold: the first aim is to compare three TLS methods for estimating PAI with  
134 traditional DHP. The second aim of this study is to use TLS to understand drivers of individual tree  $\alpha$  variation.

135 In this study we use a dataset of 528 co-located DHP and high-resolution TLS scans from 33 forest plots to  
136 compare DHP derived PAI ( $PAI_{DHP}$ ) with estimates from three methods to estimate PAI from TLS data ( $PAI_{TLS}$ ):  
137 the *LiDAR Pulse* method; the *2D Intensity Image* method and the *Voxel-Based* method (Figure 1). We use a dataset  
138 collected from a network of pine/oak forest plots in Spain (Owen et al., 2021) and ask **(1)** are the three TLS  
139 methods able to reproduce  $PAI_{DHP}$  estimates at single scan and whole plot level? **(2)** does  $\alpha$ , calculated from the  
140 *Voxel-Based* method on individual tree point clouds, vary with species and tolerance to drought? and **(3)** does  $\alpha$   
141 scale with height and stand density?

## 142 **2. Methods**

### 143 **2.1 Study site**

144 We collected TLS and DHP data from 29 plots in Alto Tajo Natural Park ([40°41'N 02°03'W](#); FunDIV – Functional  
145 Diversity plots; see Baeten et al., (2013) for a detailed description of the plots) and four plots in Cuellar  
146 ([41°23'N 4°21'W](#)) in June - July 2018 (see Owen et al., (2021) for full details) (Figure A1). Plots contained two  
147 oak species: semi-deciduous *Q. faginea* and evergreen *Q. ilex*, and three pine species: *P. nigra*, *P. pinaster* and *P.*  
148 *sylvestris*. *P. sylvestris* is the least drought tolerant species, followed by *P. nigra*, *Q. faginea*, *Q. ilex*; shade  
149 tolerance follows the same ranking (Niinemets and Valladares, 2006; Owen et al., 2021). Although not  
150 quantitatively ranked, *P. pinaster* has been shown to be very drought tolerant, appearing in drier areas than the  
151 other species (Madrigal-González et al., 2017). The area is characterised by a Mediterranean climate (altitudinal  
152 range 840 – 1400 m.a.s.l.) (Jucker et al., 2014; Madrigal-González et al., 2017). In addition to the five main canopy  
153 tree species, plots contained an understory of *Juniperus thurifera* and *Buxus sempervirens* (Kuusk et al., 2018).

### 154 **2.2 Field protocol**

155 In each of the 33 30 x 30 m plots we collected TLS scans on a 10 m grid, making 16 scan locations following  
156 Wilkes et al., (2017) to minimise occlusion effects associated with insufficient scans. We used a Leica HDS6200  
157 TLS set to super high resolution (3.1 x 3.1mm resolution at 10 m with a beam divergence of  $\leq 5$  mm at 50 m; scan  
158 time 6m 44 s; see Owen et al., (2021)). At each of the 528 scan locations and following the protocol in Pfeifer et  
159 al., (2012), we captured co-located DHP images with three exposure settings (automatic and  $\pm$  one stop exposure  
160 compensation), levelling a Canon EOS 6D full frame DSLR sensor with a Sigma EX DG F3.5 fisheye lens,  
161 mounted on a Vanguard Alta Pro 263AT tripod.

### 162 2.3 Calculation of single scan and whole plot PAI using DHP data

163 For each of the red-green-blue (RGB) DHP images we extracted the blue band for image thresholding, as this best  
164 represents sky/vegetation contrast (Pfeifer et al., 2012). For each plot, we picked the exposure setting that best  
165 represented sky/vegetation difference based on pixel brightness histograms of four sample locations indicative of  
166 the plot. We carried out automatic image thresholding using the Ridler and Calvard method (1978), to create a  
167 binary image of sky and vegetation, avoiding subjective user pixel classification (Jonckheere et al., 2005). We  
168 calculated PAI from the binary image, limiting the field of view to a  $5^\circ$  band centred on the hinge angle of  $57.5^\circ$   
169 ( $55^\circ - 60^\circ$ ). The hinge angle has a path length through the canopy twice the canopy height, so the band around it  
170 is an area of significant spatial averaging taken as representative of canopy structure of the area (Calders et al.,  
171 2018; Jupp et al., 2008). From the binarised hinge angle band we calculated  $P_{gap}$  as the number of sky pixels  
172 divided by the total number of pixels and PAI using an inverse Beer-Lambert law equation (Monsi and Saeki,  
173 1953). We calculated whole plot PAI as the arithmetic mean of the 16 plot scan location PAI estimates. As this  
174 value does not correct for canopy clumping, it is better described as effective PAI, rather than true PAI (Woodgate  
175 et al., 2015). However, as the TLS and DHP methods we apply here account for canopy clumping differently, we  
176 compared effective values and here-on refer to effective PAI as PAI (Calders et al., 2018). DHP images used in  
177 this study are freely available (see Flynn et al., 2023).

### 178 2.4 Calculation of single scan and whole plot PAI from TLS data

179 To calculate PAI using the *LiDAR Pulse* method (Jupp et al., 2008), we calculated  $P_{gap}$  for a single scan (Figure  
180 1b) by summing all returned laser pulses and dividing by the number of total outgoing pulses, following Lovell et  
181 al. (2011; see Eq. 7 in that study), and then estimated PAI following Jupp et al. (2008; see Eq. 18 in that study),  
182 setting the sensor range to  $5^\circ$  around the hinge angle as before ( $55^\circ - 60^\circ$ ). Single scan PAI was taken as the  
183 cumulative sum of PAI values estimated by vertically dividing the hinge region into 25 cm intervals (Calders et  
184 al., 2014). We implemented the *LiDAR Pulse* method using the open-source *R* (R Core Team, 2020) package,  
185 *rTLS* (Guzmán and Hernandez, 2021).

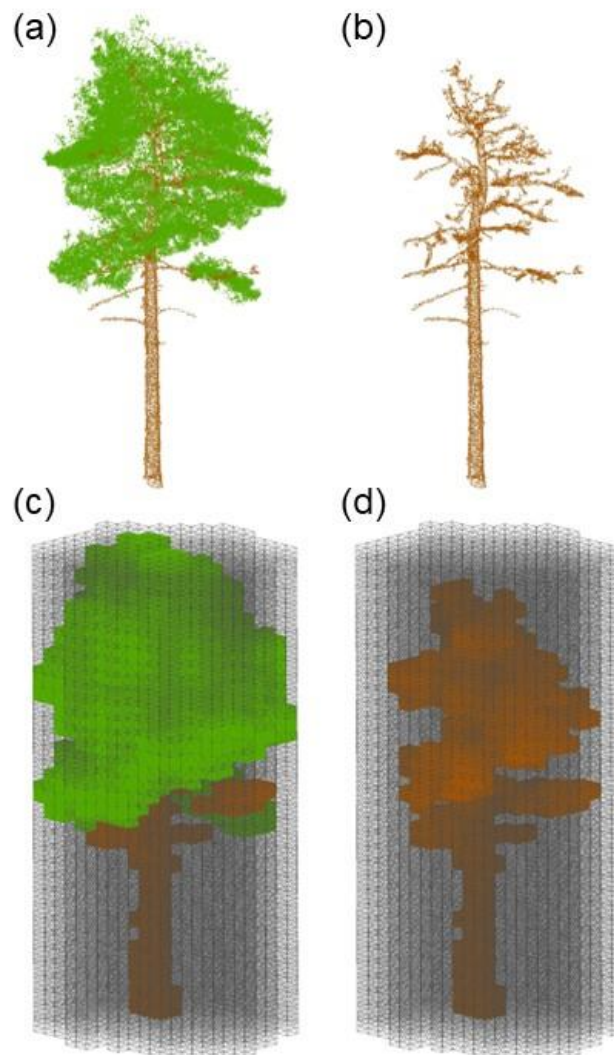
186 To calculate PAI using the *2D Intensity Image* method (Zheng et al., 2013), we converted 3D TLS point cloud  
187 data from all 528 scan locations into polar coordinates, scaled intensity values to cover the full 0-255 range (Figure  
188 1c) and rasterised into a 2D intensity image using the open-source *R* package, *raster* (Hijmans, 2022). We cut the  
189 2D intensity image to a  $5^\circ$  band around the hinge angle ( $55^\circ - 60^\circ$ ) and classified sky and vegetation pixels in each  
190 image using the Ridler and Calvard method (1978). We calculated  $P_{gap}$  as the number of pixels classified as sky  
191 divided by the total number of pixels and derived PAI with an inverse Beer-Lambert law equation (Monsi and  
192 Saeki, 1953).

193 Following the same approach as applied to our DHP data, we calculated whole plot PAI for the *LiDAR Pulse* and  
194 *2D Intensity Image* methods as the arithmetic mean of the 16 plot scan location PAI estimates.

195 To calculate PAI using the *Voxel-Based* method, we followed a voxel classification approach (Hosoi and Omasa,  
196 2006), downsampling the point cloud to 0.05 m to aid computation time and matching the voxel size to the  
197 resolution of the point cloud, following Li et al., (2016), who showed that matching the voxel size to the point  
198 cloud point to point minimum distance (resolution) increases accuracy as small canopy gaps are not included in  
199 voxels classified as vegetation. We chose to use a voxel classification approach (rather than a radiative transfer

200 based one) as this method is widely applicable to a range of TLS systems and levels of processing, as well as  
201 providing explicit guidance on voxel size selection, which is known to impact derived PAI estimates (Li et al.,  
202 2016). We re-combined individually segmented trees, filtered for noise using a height-dependent statistical filter  
203 (see Owen et al., 2021) back into whole plot point clouds and voxelised them using the open source R package,  
204 *VoxR* (Lecigne et al., 2018), with a full grid covering the minimum to maximum XYZ ranges of the plot. We  
205 classified any voxel containing  $> 0$  points as vegetation (“filled”), and empty voxels as gaps. We then split the  
206 voxelised point cloud vertically into slices one voxel high. Within each slice, the contact frequency is calculated  
207 as the fraction of filled to total number of voxels. We then multiplied the contact frequency by a correction factor  
208 for leaf inclination, set at 1.1 (Li et al., 2017), and whole plot PAI was calculated as the sum of all slices’ contact  
209 frequencies.

## 210 2.5 Calculation of individual tree PAI, WAI and $\alpha$ using the voxel-based method



211 **Figure 2: Visualisation of the workflow for applying the Voxel-Based method to estimate individual-tree PAI, WAI and**  
212  **$\alpha$ .** (a) Individual tree point cloud; (b) separated leaf off (wood) individual tree point cloud; (c) voxelised individual tree  
213 **point cloud; (d) voxelised wood cloud. Coloured voxels (green represents leaf and brown represents wood) are filled**  
214 **voxels and grey lines are empty voxels. Empty voxels occupy the space within the projected crown area of the tree.**  
215 **Image shows schematic of point cloud voxelised with cube voxels with edge length of 0.5 m. Panels (a) and (b) show**  
216 **wood and leaf separation of an example *P. sylvestris*, carried out using *TLSeparation* (Vicari et al., 2019). Point cloud**

217 voxelisation was carried out using modified functions from R package *VoxR* (Lecigne et al., 2018). Note that our method  
218 used voxel sizes at the resolution of the cloud (5 cm), but here we present an image with larger voxels to ease visual  
219 interpretation.

220 As the only method using multiple co-registered scans, the *Voxel-Based* method is only method compared in this  
221 study capable of deriving PAI, WAI and LAI of segmented individual tree point clouds. We estimated PAI and  
222 WAI for 2472 individual trees segmented from co-registered point clouds following a similar method to the whole  
223 plot point cloud. We used individual tree point clouds downsampled to 0.05 m, to aid computation time, and  
224 segmented using the automated tree segmentation program *treeseq* (Burt et al., 2019), implemented in C++, by  
225 Owen et al., (2021) for that study. Individual segmented tree data used in this study are freely available (see Owen  
226 et al., 2022).

227 To estimate PAI, WAI and  $\alpha$  for each tree, we used individual tree point clouds wood – leaf separated by Owen  
228 et al., (2021) using the open source Python library *TLSeparation* (Vicari et al., 2019), and then used the separated  
229 wood point clouds to calculate WAI. *TLSeparation* assigns points as either leaf or wood, iteratively looking at a  
230 predetermined number of nearest neighbours (*knn*). The *knn* of each iteration is directly dependent on point cloud  
231 density, since high density point clouds will require higher a *knn* (Vicari et al., 2019). The utility package in  
232 *TLSeparation* was used to automatically detect the optimum *knn* for each tree point cloud.

233 To voxelise individual tree complete (Figure 2a) and wood only (Figure 2b) point clouds, we used a modified  
234 approach based on Lecigne et al., (2018), voxelising within the projected crown area of the whole tree point cloud  
235 (Figure 2c) to calculate PAI. In the same way as for PAI, we calculated WAI using the separated wood point cloud  
236 within the projected crown area of the whole tree (Figure 2d; using the whole crown and not just the wood point  
237 cloud), and derived  $\alpha$  for each tree as  $WAI/PAI$ , allowing a comparison with existing literature estimating  $\alpha$  for a  
238 range of ecosystems, (Sea et al., 2011; Woodgate et al., 2016).

## 239 2.6 Statistical Analyses

240 We tested the relationships between  $PAI_{TLS}$  and  $PAI_{DHP}$  estimates using Standardised Major Axis (SMA) using  
241 the open source R (R Core Team, 2020) package, *smatr* (Warton et al., 2012). SMA is an approach to estimating  
242 a line of best fit where we are not able to predict one variable from another (Warton et al., 2006); we chose SMA  
243 because we do not have a ‘true’ validation dataset, so avoid assuming either DHP or any of the TLS methods  
244 produces the most accurate results. For each TLS method, we assessed the relationship with DHP using the  
245 coefficient of determination and RMSE. We chose to compare PAI values rather than WAI or LAI as to do so  
246 would mean an additional correction for non-photosynthetic elements, which each method does in different ways,  
247 so introducing further source of uncertainty and limiting our ability to fairly compare processing approaches. To  
248 further understand observed drivers of variance in PAI, we tested the relationship between PAI and whole plot  
249 crown area index, CAI, a proxy measure of stand density and local competition (Caspersen et al., 2011; Coomes  
250 et al., 2012). We calculated CAI as the sum of TLS-derived projected crown area, divided by the plot area (Owen  
251 et al., 2021).

252

253 To test if  $\alpha$  differs by species, we used linear mixed models (LMMs) in the R package, *lme4* (Bates et al., 2015).  
254 We included an intercept only random plot effect to account for local effects on  $\alpha$ :



255

$$256 \quad \alpha_{i,sj} = a_s + Plot_j \quad (1)$$

257

258 here,  $\alpha_i$  is  $\alpha$  of an individual of species  $s$ , in plot  $j$ , and  $a_s$  is the parameter to be fit. To test the effect of stand  
259 structure and tree height on  $\alpha$ , we fit relationships separately for each species, again including a random plot  
260 effect:

261

$$262 \quad \alpha_{i,sj} = a_s + b_s H_i + c_s CAI_j + Plot_{sj} \quad (2)$$

263

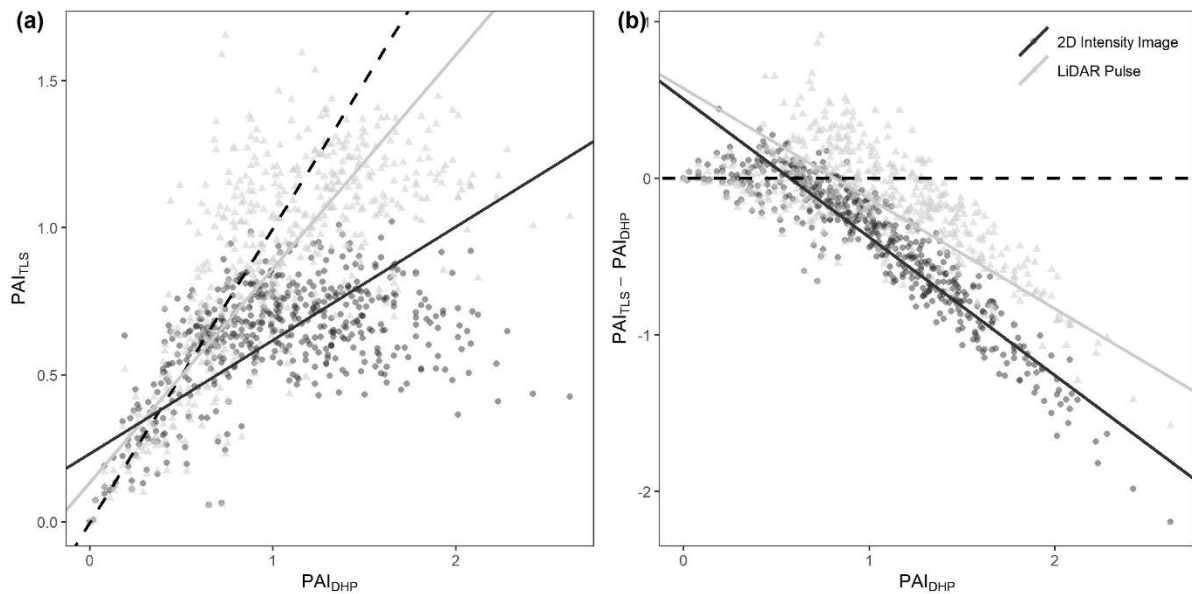
264 here  $H_i$  is the height of the tree,  $CAI_j$  is the crown area index for the plot, with other parameters as before.

265 For each species' model (equation 2), we calculated the intra-class correlation coefficient (ICC). The ICC, similar  
266 to coefficient of determination, quantifies the amount of variance explained by the random effect in a linear mixed  
267 model (Nakagawa et al., 2017).

### 268 **3. Results**

#### 269 **3.1 Comparison of plant area index estimated by DHP and single scan TLS**

270 Of the two single scan TLS methods tested (*LiDAR Pulse* method and *2D Intensity Image* method), we found that  
271 the relationship between PAI estimated using the *LiDAR Pulse* method and  $PAI_{DHP}$ , had a higher  $R^2$  than the *2D*  
272 *Intensity Image* method (SMA; *LiDAR Pulse* method  $R^2 = 0.50$ , slope = 0.73,  $p < 0.001$ , RMSE = 0.14, and *2D*  
273 *Intensity Image* method  $R^2 = 0.22$ , slope = 0.38,  $p < 0.001$ , RMSE = 0.39, respectively, Figure 3a). At larger PAI  
274 values, both TLS methods underestimated PAI relative to DHP (Figure 3b). We found statistically significant  
275 negative correlations between residuals and DHP for both methods (SMA; *2D Intensity Image* method residuals  
276  $R^2 = 0.85$ , slope = -0.88,  $p < 0.01$ ; *LiDAR Pulse* method residuals  $R^2 = 0.47$ , slope = -0.70,  $p < 0.01$ ; Figure 3b). The  
277 *2D Intensity Image* method showed larger underestimation at higher  $PAI_{DHP}$  values, suggesting this method may  
278 saturate sooner for higher PAI values than either DHP or the *LiDAR Pulse* method (Figure 3b).



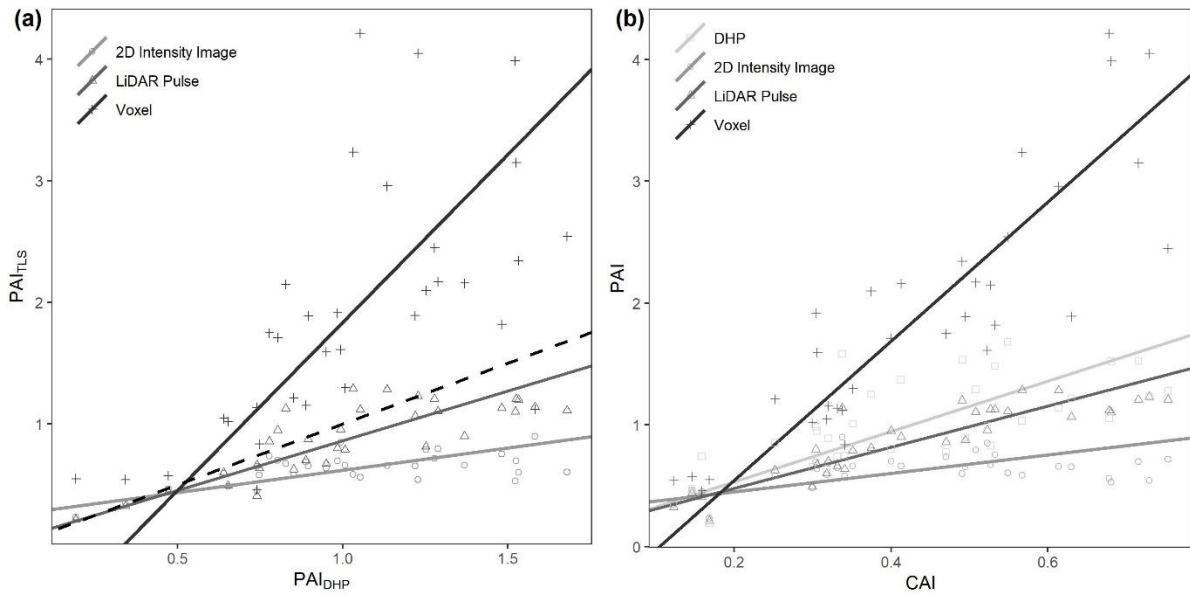
279

280 **Figure 3: Comparison of single scan  $PAI_{TLS}$  and  $PAI_{DHP}$  estimates, for all 528 scan locations (16 per plot). (a) The**  
 281 **correlation between DHP derived PAI with PAI derived using the 2D Intensity Image method  $R^2 = 0.22$ , slope = 0.38,**  
 282  **$p < 0.001$ , RMSE = 0.39 (circles), and LiDAR Pulse method  $R^2 = 0.50$ , slope = 0.73,  $p < 0.001$ , RMSE = 0.14 (triangles).**  
 283 **Dashed line in panel (a) represents 1:1 relationship. (b) The difference between  $PAI_{TLS}$  and  $PAI_{DHP}$  estimates for the**  
 284 **2D Intensity Image method, and LiDAR Pulse method. Dashed line in panel (b) represents 0. Lines show statistically**  
 285 **significant relationships fitted using SMA ( $p < 0.01$ ).**

### 286 3.2 Comparison of whole plot plant area index estimated using TLS and DHP and the effect of plot structure 287 on PAI

288 We found statistically significant correlations between whole plot  $PAI_{TLS}$  values and  $PAI_{DHP}$  for all three TLS  
 289 methods (Figure 4). As for single scans, the *LiDAR Pulse* method showed the closest agreement to  $PAI_{DHP}$ , here  
 290 compared to both the *Voxel-Based* and *2D Intensity Image* methods (SMA; *LiDAR Pulse* method  $R^2 = 0.66$ , slope  
 291 = 0.82,  $p < 0.01$ , RMSE = 0.14; *Voxel-Based* method  $R^2 = 0.39$ , slope = 2.76,  $p < 0.01$ , RMSE = 0.88; *2D Intensity*  
 292 *Image* method  $R^2 = 0.35$ , slope = 0.36,  $p < 0.01$ , RMSE = 0.39, respectively; Figure 4a). The *2D Intensity Image*  
 293 method and *LiDAR Pulse* method consistently underestimated PAI compared to DHP, whilst the *Voxel-Based*  
 294 method underestimated in plots with lower  $PAI_{DHP}$  and overestimated in plots with higher  $PAI_{DHP}$ . The *Voxel-*  
 295 *Based* method's high PAI values compared to other methods is likely due to its use of multiple co-registered scans  
 296 reducing occlusion effects prevalent in single scan data.

297 To assess the effect of plot structure on variation in TLS derived PAI, we compared  $PAI_{TLS}$  estimates to TLS  
 298 estimated crown area index (CAI,  $m^2$  projected crown area per  $m^2$  ground area, Figure 4b). We found a significant  
 299 positive relationship between CAI and PAI estimated using each of the *LiDAR Pulse* method, the *Voxel-Based*  
 300 method, and DHP (SMA; *LiDAR Pulse* method  $R^2 = 0.79$ , slope = 1.69,  $p < 0.01$ ; *Voxel-Based* method  $R^2 = 0.76$ ,  
 301 slope = 5.72,  $p < 0.01$ ; *2D Intensity Image* method  $R^2 = 0.15$ , slope = 0.76,  $p < 0.05$ ; DHP  $R^2 = 0.46$ , slope = 2.07,  
 302  $p < 0.01$ , respectively; Figure 4b), where the *2D Intensity Image* method shows signs of saturation at medium CAI  
 303 values (Figure 4b).

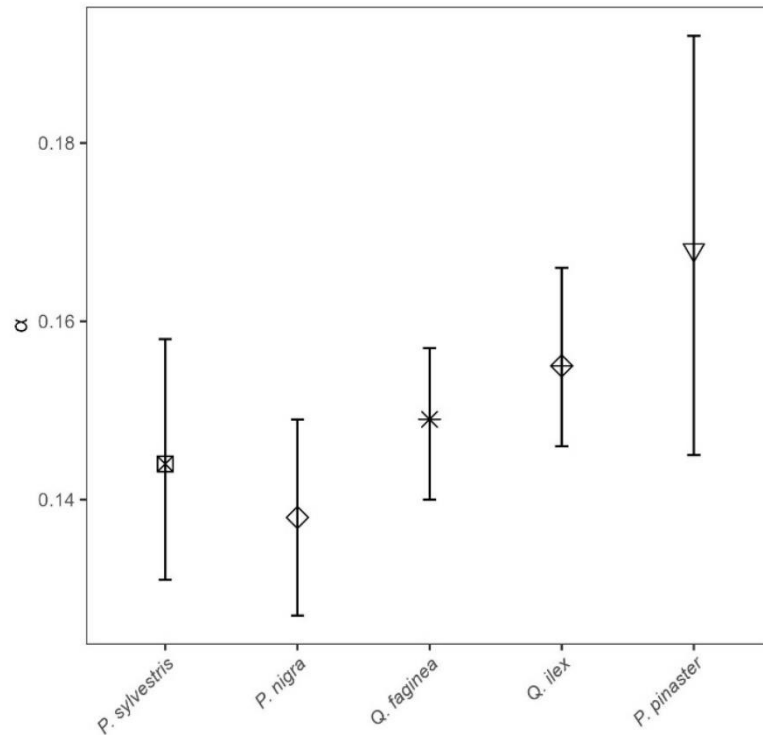


304

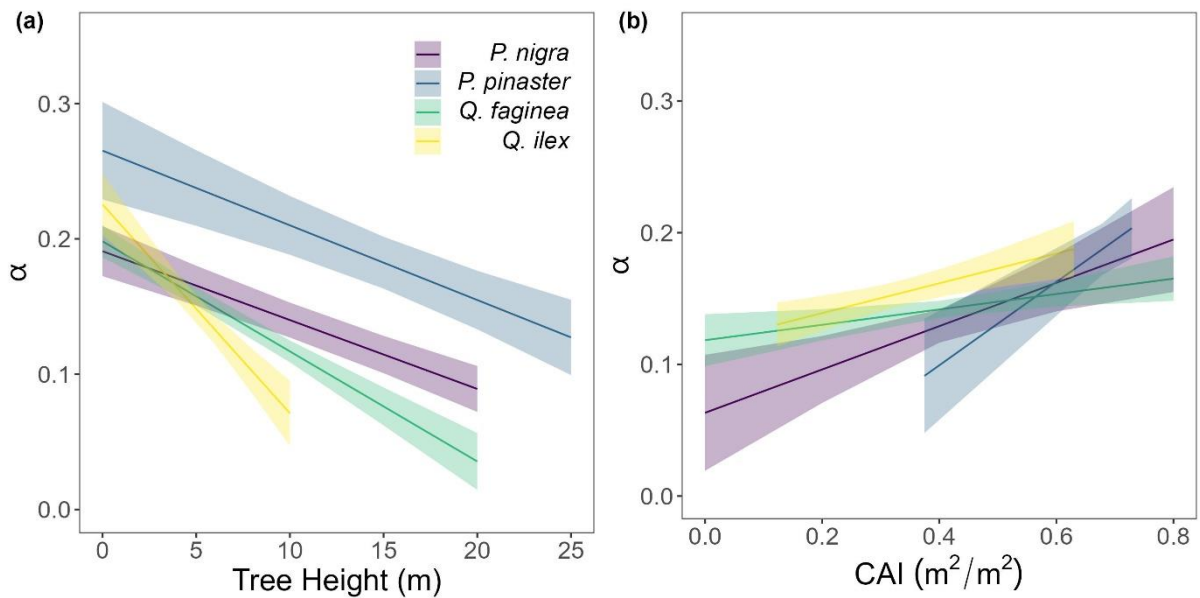
305 **Figure 4: Comparison of plot level PAITLS vs PAIDHP, and CAI vs PAI estimates for all 33 plots. (a) The correlation**  
 306 **between DHP derived PAI and PAI derived using 2D Intensity Image  $R^2 = 0.35$ , slope = 0.36,  $p < 0.01$ , RMSE = 0.39**  
 307 **(circle), LiDAR Pulse  $R^2 = 0.66$ , slope = 0.82,  $p < 0.01$ , RMSE = 0.14 (triangle) and Voxel-Based  $R^2 = 0.39$ , slope = 2.76,**  
 308  **$p < 0.01$ , RMSE = 0.88 (cross) methods (b) The correlation between TLS derived CAI and PAI derived using DHP  $R^2 =$**   
 309 **0.46, slope = 2.07,  $p < 0.01$  (square), 2D Intensity Image  $R^2 = 0.15$ , slope = 0.76,  $p < 0.05$  (circle) LiDAR Pulse  $R^2 = 0.79$ ,**  
 310 **slope = 1.69,  $p < 0.01$  (triangle) and Voxel-Based  $R^2 = 0.76$ , slope = 5.72,  $p < 0.01$  (cross) methods. Lines show statistically**  
 311 **significant relationships fitted using SMA ( $p < 0.01$ ). Dashed line in panel (a) represents 1:1 relationship.**

### 312 3.4 Influence of species, tree height and CAI on $\alpha$

313 To understand drivers of variance in  $\alpha$ , we used individual tree PAI and WAI, calculated using the *Voxel-Based*  
 314 method to test the relationship between species and  $\alpha$ , and height/ CAI and  $\alpha$ . We found that more drought tolerant  
 315 species generally had higher  $\alpha$  values than less drought tolerant species (Table B1; Figure 5), however, confidence  
 316 intervals were wide and overlapping, suggesting that species is not a strong predictor of variation in  $\alpha$ . We found  
 317 a statistically significant negative effect of height ( $p < 0.001$ ; Table B2; Figure 6a) and positive effect of CAI  
 318 ( $p < 0.01 - 0.05$ ; Table B2; Figure 6b) on  $\alpha$  for all species apart from *P. sylvestris*.  $\alpha$  decreased more rapidly with  
 319 height and increased less rapidly with CAI for oaks than pines. Statistically significant ICC values were higher  
 320 for *P. nigra* (ICC = 0.211; Table B2) than *P. pinaster*, *Q. faginea* and *Q. ilex* (ICC = 0.036; 0.060; 0.070,  
 321 respectively), showing that more  $\alpha$  variation is explained by the random plot effect in *P. nigra* than the other  
 322 species. *P. pinaster* has a wider confidence interval (Figure 5), possibly explained by its lower sample size. To  
 323 understand drivers of variance in WAI we carried out additional analysis to test the relationship between WAI  
 324 and species, height, CAI and PAI, and presented these results in Appendix C (Figure C3; Tables C3, C4).



325 **Figure 5:** Linear mixed model derived  $\alpha$  values (a, equation 1) for all 2472 individual trees of species *P. sylvestris*, *P.*  
 326 *nigra*, *Q. faginea*, *Q. ilex* and *P. pinaster*. Error bars represent 95% confidence intervals. Species are listed left to right  
 327 from low – high drought tolerance, with the exception of *P. pinaster*, for which drought tolerance index has not been  
 328 calculated in the literature. Drought tolerance rankings are taken from Niinemets and Valladares, (2006).



329 **Figure 6:** Variation in  $\alpha$  for each species: *Pinus nigra*, *P. pinaster*, *Q. faginea* and *Q. ilex* with (a) height and (b) plot  
 330 CAI. Lines represent statistically significant linear mixed models (equation 2; significance levels from  $p < 0.001$  to  $p <$   
 331  $0.05$ ). Ribbons represent 95% confidence intervals. The model for *P. sylvestris* was not statistically significant.

332  
 333  
 334

## 335 4. Discussion

### 336 4.1 Comparison of approaches to deriving PAI from remote sensed data

337 We found substantial differences in PAI values estimated from TLS and DHP and from different TLS processing  
338 methods (Figures 3 and 4). Further, differences between TLS methods varied across plot structure (CAI), with the  
339 greatest differences between methods in plots with high CAI, and therefore high canopy density. Although  
340 previous studies have presented TLS as an improvement over DHP due to its independence of illumination and  
341 sky conditions during the data acquisition phase, and ability to resolve fine-scale canopy elements and gaps  
342 (Calders et al., 2018; Grotti et al., 2020; Zhu et al., 2018), we have shown that there is large variability between  
343 TLS processing methods in Mediterranean forests. Rigorous intercomparison of approaches, ideally using  
344 standard benchmarking TLS datasets, and destructive sampling, would improve trust and reliability of TLS  
345 algorithms.

346 We found the *LiDAR Pulse* method (Jupp et al., 2008) to have the best agreement with DHP for both whole plot  
347 and single scan PAI estimates. In contrast to previous studies comparing  $PAI_{TLS}$  with  $PAI_{DHP}$  (Calders et al.,  
348 2018; Grotti et al., 2020; Woodgate et al., 2015), we found that the *LiDAR Pulse* and *2D Intensity Image* methods  
349 underestimated PAI compared to DHP, except at very low PAI values ( $PAI_{TLS} < 0.5$ ). Quantification of PAI from  
350 DHP may introduce additional sources of error, for example, its relatively lower resolution compared to TLS  
351 could lead to mixed pixels that have a greater chance of misclassification of sky as vegetation (Jonckheere et al.,  
352 2004). This effect could be enhanced in a Mediterranean forest as trees in drier climates tend to have smaller  
353 leaves (Peppe et al., 2011), leading to more small canopy gaps that TLS may resolve where DHP cannot. Further,  
354 although we took steps to reduce the error introduced at DHP data acquisition and processing steps, including  
355 using automatic thresholding and collecting images with multiple exposures, DHP processing requires both model  
356 and user assumptions that can impact results. For example,  $PAI_{DHP}$  estimates are highly sensitive to camera  
357 exposure; increasing one stop of exposure can result in 3 – 28% difference in PAI and use of automatic exposure  
358 can result in up to 70% error (Zhang et al., 2005).

359 We found the *Voxel-Based* method overestimated PAI values compared to the other methods at the whole plot  
360 level. This is likely due to the method's use of co-registered scans, rather than averaged single scan PAI values,  
361 since co-registered scans will reduce occlusion effects prevalent in single scan data that could lead to an  
362 underestimation of PAI (Wilkes et al., 2017). The *Voxel-Based* method is, however, sensitive to voxel size (Li et  
363 al., 2016), and larger voxels lead to larger PAI estimates as they fill small canopy gaps; we chose a voxel size of  
364 0.05 m to match the minimum distance between points in our downsampled dataset. However, the *Voxel-Based*  
365 method is a memory intensive approach to calculating PAI, and smaller voxels have higher memory requirements.  
366 We picked this data resolution, and therefore voxel size, to balance the need to capture fine-scale canopy details  
367 against memory requirements for running the method on many large plot point clouds. Voxel size could have been  
368 chosen based on estimates' match to DHP, but this would assume (1) that DHP estimates are most accurate, and  
369 (2) that DHP data are always available, limiting the wider applicability of our findings. Understanding which  
370 method is over- or underestimating would require a destructively sampled dataset for validation, which was not  
371 possible for this study (or most ecosystems). However, other studies using voxel approaches have found that  
372 although these produce high LAI values for individual trees, these are underestimates compared with destructive  
373 samples (Li et al., 2016). Regardless, PAI and LAI estimates using a *Voxel-Based* approach are highly dependent

374 on voxel size (Li et al., 2016), and future work should test the influence of voxel size on PAI estimates, using  
375 destructive samples in a range of environments.

376 The relationship between the *LiDAR Pulse* method and TLS derived CAI had the highest  $R^2$ , demonstrating that  
377 the method is well suited to measuring PAI across the range of plot CAI values used in this study. Although the  
378 *2D Intensity Image* method can tackle the significant challenges presented by edge effects and partial beam  
379 interceptions, particularly present in phase-shift systems (Grotti et al., 2020), our results suggest this method has  
380 a lower performance ability, with saturation occurring sooner than all other methods in dense forests (Figures 3  
381 and 4). The *2D Intensity Image* method uses the same raw single scan data as the *LiDAR Pulse* method, so the  
382 better performance from the latter is likely due to the method's use of vertically resolved gap fraction; both the  
383 *LiDAR Pulse* method and *Voxel-Based* method account for the vertical structure of the canopy by summing  
384 vertical slices through the canopy.

#### 385 **4.2 $\alpha$ variation between species and plot**

386 We used the *Voxel-Based* method to investigate individual tree  $\alpha$  variation between species and across structure,  
387 as this was the only approach we compared that could be applied to single tree point clouds which are leaf-wood  
388 separated. We found  $\alpha$  values obtained were within the range of values obtained from destructive approaches (0.1  
389 – 0.6, Gower et al., 1997). The drought and shade intolerant *P. nigra* showed stronger variability in  $\alpha$  across plots  
390 (higher ICC value, Table B2) than other species, suggesting its wood – leaf ratio may be more sensitive to site  
391 factors. However, as the plots measured in this study vary in both abiotic conditions (altitude, aspect, slope,  
392 wetness) as well as species composition, stem density and canopy cover, there may be other drivers of variation  
393 in  $\alpha$  values.

394 We found some evidence that species with higher drought tolerance had higher  $\alpha$  values (Figure 5; Table B1),  
395 however, confidence intervals were wide, suggesting a weak relationship. There is evidence that trees that tolerate  
396 water limited environments have a lower leaf area (Battaglia et al., 1998; Mencuccini and Grace, 1995), so higher  
397  $\alpha$  values may reflect maintenance of homeostasis of leaf water use through adjustment of wood to leaf area ratio  
398 (Carter and White, 2009; Gazal et al., 2006). The potential for a tree to lose water is mostly regulated through leaf  
399 traits including stomatal conductance and leaf area, and both stand (Battaglia et al., 1998; Specht and Specht,  
400 1989) and individual tree (Mencuccini, 2003) water use have been found to scale linearly with LAI, with drought  
401 often mitigated through leaf shedding (López et al., 2021).

#### 402 **4.3 Tree stature and stand density drives $\alpha$ variation**

403 Although species had a weak relationship with  $\alpha$ , tree height and plot CAI had a statistically significant  
404 relationship with  $\alpha$  ( $p < 0.001$  –  $p < 0.05$ ) for all species, showing the importance of local stand structure on leaf and  
405 woody allocation. We found that  $\alpha$  scaled negatively with height for all species apart from *P. sylvestris*, suggesting  
406 that in this environment, taller trees generally have a lower proportion of wood to plant area index than shorter  
407 ones. *P. sylvestris*, which is at the edge of its geographical range and physiological limits (Castro-Díez et al.,  
408 1997; Owen et al., 2021), showed no significant relationship between height and  $\alpha$ . We found that  $\alpha$  scaled  
409 positively with plot level CAI for all species apart from *P. sylvestris*, that is, trees growing in denser plots have a  
410 higher  $\alpha$ . This supports theory that trees growing in dense forests are competing for resources, reducing individual  
411 tree leaf area (Jump et al., 2017). The negative height –  $\alpha$  and positive CAI –  $\alpha$  relationships in our model suggest

412 that trees may initially invest in vertical growth to reach the canopy level, and once there invest in lateral growth,  
413 with more leaf area, to increase light capture. This supports theory that trees grow to outcompete neighbouring  
414 individuals for light capture (Purves and Pacala, 2008) and evidence that both lateral growth and LAI are reduced  
415 beneath closed canopies (Beaudet and Messier, 1998; Canham, 1988).

416 Wood may be harder to accurately classify than leaves in TLS data (Vicari et al., 2019), resulting in a higher  
417 occurrence of false positives in wood clouds, potentially leading to an overestimation in WAI, and therefore  
418 underestimation of  $\alpha$ , especially in trees with small leaves which are prevalent in dry, Mediterranean environments  
419 (Peppe et al., 2011). The problem of misclassification will increase in taller trees due to TLS beam divergence,  
420 occlusion and larger beam footprint at further distances (Vicari et al., 2019), suggesting that WAI overestimation  
421 could be more pronounced in tall trees. Although our dense scanning strategy (Owen et al., 2021) was designed  
422 to mitigate some of these effects, these effects mean our findings may underestimate the slope of the negative  
423 relationship between  $\alpha$  and tree height.

#### 424 **4.4 Correcting for non-photosynthetic elements in LAI estimates using TLS**

425 The value of TLS data to estimate individual tree PAI, WAI and subsequently  $\alpha$ , demonstrates their potential to  
426 corrective factors for non-photosynthetic components in ground based remote sensing measurements of LAI.  
427 Properly correcting for WAI in LAI estimates is of global importance as small errors in ground based  
428 measurements propagate through to large scale satellite observations generating large errors in global vegetation  
429 models (Calders et al., 2018). The work presented here provides a foundation for future work combining multi-  
430 source and multi-scale remote sensing datasets to correct largescale LAI products. Our results echo others' in  
431 finding that the prevalence of woody material in the tree canopy, and therefore  $\alpha$ , is dynamic and varies by species  
432 as well as senescence, crown health and, in the case of deciduous forests, leaf phenology (Gower et al., 1999).  
433 The use of single  $\alpha$  value in a plot or region (Olivas et al., 2013; Woodgate et al., 2016), invariant of species, size  
434 and forest structure, to convert PAI to LAI is therefore problematic (Niu et al., 2021). Our study demonstrates the  
435 importance of taking species mix and structural variation into account when correcting for non-photosynthetic  
436 material in ground-based LAI estimates.

#### 437 **5. Conclusions**

438 We tested three methods for estimating PAI using Terrestrial Laser Scanning data and compared these against  
439 traditional DHP measurements. We found large variation between PAI values estimated from each TLS method  
440 and DHP, demonstrating that care should be taken when deriving PAI from ground based remote sensing methods.  
441 Although the *LiDAR Pulse* method was found to have the best agreement with both single scan and whole plot  
442 PAI values measured by DHP, the *Voxel-Based* method allowed separate analysis of the key metric used to correct  
443 for the effect of WAI in LAI measurements,  $\alpha$ , in individual trees. We recommend the *LiDAR Pulse* method as a  
444 fast and effective method for PAI estimation independent of illumination conditions. Whilst the *Voxel-Based*  
445 method may be used to analyse individual tree  $\alpha$  and determine ecological drivers of variation, work remains to  
446 determine the validity of these approaches, in particular correct voxel size choice. We found that  $\alpha$  varies by  
447 species, height and stand density, showing the importance of accurately correcting for WAI on the individual tree  
448 level and the utility of TLS to do so.

449 The variation in our results for the different methods used to derive PAI from TLS data show that there is some  
450 way to go before TLS derived vegetation indices can be interpreted as robust and reliable. Validation using  
451 destructive samples and further intercomparison studies of methods are needed to demonstrate the advantages of  
452 TLS, and use of benchmarking datasets should be standard. DHP is a faster, cheaper and more widely accessible  
453 method for PAI estimation, and while TLS promises to alleviate potential bias in DHP estimates, results are highly  
454 methods dependent. Our results demonstrate the challenges that stand in the way of large scale adoption of TLS  
455 for vegetation indices monitoring.

## 456 **6. Code availability**

457 See [https://github.com/will-flynn/tls\\_dhp\\_pai.git](https://github.com/will-flynn/tls_dhp_pai.git) for all processing and modelling code.

## 458 **7. Data availability**

459 See Owen et al., (2022) for individual segmented tree data and Flynn et al., (2023) for thresholded DHP images.

## 460 **8. Author contribution**

461 All authors designed the study. HJFO and WRMF collected and processed TLS and DHP data; WRMF performed  
462 formal analysis with guidance from all authors. WRMF led the writing with input from all authors. All authors  
463 contributed critically to drafts and gave final approval for publication.

## 464 **9. Competing interests**

465 The authors declare that they have no conflict of interest.

## 466 **7. Acknowledgements**

467 WRMF was funded through a London NERC DTP PhD studentship. ERL, HJFO and SWDG were funded through  
468 the UKRI Future Leaders Fellowship awarded to ERL (MR/T019832/1).

## 469 **References**

- 470 Baeten, L., Verheyen, K., Wirth, C., Bruelheide, H., Bussotti, F., Finér, L., Jaroszewicz, B., Selvi, F.,  
471 Valladares, F., Allan, E., Ampoorter, E., Auge, H., Avăcăriei, D., Barbaro, L., Bărnoaiea, I., Bastias, C. C.,  
472 Bauhus, J., Beinhoff, C., Benavides, R., Benneter, A., Berger, S., Berthold, F., Boberg, J., Bonal, D.,  
473 Brüggemann, W., Carnol, M., Castagneyrol, B., Charbonnier, Y., Chečko, E., Coomes, D., Coppi, A., Dalmaris,  
474 E., Dănilă, G., Dawud, S. M., de Vries, W., De Wandeler, H., Deconchat, M., Domisch, T., Duduman, G.,  
475 Fischer, M., Fotelli, M., Gessler, A., Gimeno, T. E., Granier, A., Grossiord, C., Guyot, V., Hantsch, L.,  
476 Hättenschwiler, S., Hector, A., Hermy, M., Holland, V., Jactel, H., Joly, F.-X., Jucker, T., Kolb, S., Koricheva,  
477 J., Lexer, M. J., Liebergesell, M., Milligan, H., Müller, S., Muys, B., Nguyen, D., Nichiforel, L., Pollastrini, M.,  
478 Proulx, R., Rabasa, S., Radoglou, K., Ratcliffe, S., Raulund-Rasmussen, K., Seiferling, I., Stenlid, J., Vesterdal,  
479 L., von Wilpert, K., Zavala, M. A., Zielinski, D., and Scherer-Lorenzen, M.: A novel comparative research  
480 platform designed to determine the functional significance of tree species diversity in European forests,  
481 *Persepect. Plant. Ecol.*, 15, 281–291, <https://doi.org/10.1016/j.ppees.2013.07.002>, 2013.
- 482 Baret, F., Weiss, M., Lacaze, R., Camacho, F., Makhmara, H., Pacholczyk, P., and Smets, B.: GEOV1: LAI and  
483 FAPAR essential climate variables and FCOVER global time series capitalizing over existing products. Part1:  
484 Principles of development and production, *Remote Sens. Environ.*, 137, 299–309,  
485 <https://doi.org/10.1016/j.rse.2012.12.027>, 2013.
- 486 Bates, D., Mächler, M., Bolker, B., and Walker, S.: Fitting Linear Mixed-Effects Models Using lme4, *J. Sat.*  
487 *Softw.*, 67, <https://doi.org/10.18637/jss.v067.i01>, 2015.
- 488 Battaglia, M., Cherry, M. L., Beadle, C. L., Sands, P. J., and Hingston, A.: Prediction of leaf area index in  
489 eucalypt plantations: effects of water stress and temperature, *Tree Physiol.*, 18, 521–528,  
490 <https://doi.org/10.1093/treephys/18.8-9.521>, 1998.



- 491 Beaudet, M. and Messier, C.: Growth and morphological responses of yellow birch, sugar maple, and beech  
492 seedlings growing under a natural light gradient, *Can. J. Forest Res.*, 28, 1007–1015,  
493 <https://doi.org/10.1139/x98-077>, 1998.
- 494 Béland, M., Baldocchi, D. D., Widlowski, J.-L., Fournier, R. A., and Verstraete, M. M.: On seeing the wood  
495 from the leaves and the role of voxel size in determining leaf area distribution of forests with terrestrial LiDAR,  
496 *Agr. Forest Meteorol.*, 184, 82–97, <https://doi.org/10.1016/j.agrformet.2013.09.005>, 2014.
- 497 Breda, N. J. J.: Ground-based measurements of leaf area index: a review of methods, instruments and current  
498 controversies, *J. Exp. Bot.*, 54, 2403–2417, <https://doi.org/10.1093/jxb/erg263>, 2003.
- 499 Burt, A., Disney, M., and Calders, K.: Extracting individual trees from lidar point clouds using treeSeg, *Methods*  
500 *Ecol. Evol.*, 10, 438–445, <https://doi.org/10.1111/2041-210X.13121>, 2019.
- 501 Calders, K., Armston, J., Newnham, G., Herold, M., and Goodwin, N.: Implications of sensor configuration and  
502 topography on vertical plant profiles derived from terrestrial LiDAR, *Agr. Forest Meteorol.*, 194, 104–117,  
503 <https://doi.org/10.1016/j.agrformet.2014.03.022>, 2014.
- 504 Calders, K., Origo, N., Disney, M., Nightingale, J., Woodgate, W., Armston, J., and Lewis, P.: Variability and  
505 bias in active and passive ground-based measurements of effective plant, wood and leaf area index, *Agr. Forest*  
506 *Meteorol.*, 252, 231–240, <https://doi.org/10.1016/j.agrformet.2018.01.029>, 2018.
- 507 Calders, K., Adams, J., Armston, J., Bartholomeus, H., Bauwens, S., Bentley, L. P., Chave, J., Danson, F. M.,  
508 Demol, M., Disney, M., Gaulton, R., Krishna Moorthy, S. M., Levick, S. R., Saarinen, N., Schaaf, C., Stovall,  
509 A., Terryn, L., Wilkes, P., and Verbeeck, H.: Terrestrial laser scanning in forest ecology: Expanding the  
510 horizon, *Remote Sensing of Environment*, 251, 112102, <https://doi.org/10.1016/j.rse.2020.112102>, 2020.
- 511 Canham, C. D.: Growth and Canopy Architecture of Shade-Tolerant Trees: Response to Canopy Gaps, *Ecology*,  
512 69, 786–795, <https://doi.org/10.2307/1941027>, 1988.
- 513 Carter, J. L. and White, D. A.: Plasticity in the Huber value contributes to homeostasis in leaf water relations of  
514 a mallee Eucalypt with variation to groundwater depth, *Tree Physiol.*, 29, 1407–1418,  
515 <https://doi.org/10.1093/treephys/tpp076>, 2009.
- 516 Caspersen, J. P., Vanderwel, M. C., Cole, W. G., and Purves, D. W.: How Stand Productivity Results from Size-  
517 and Competition-Dependent Growth and Mortality, *PLoS ONE*, 6, e28660,  
518 <https://doi.org/10.1371/journal.pone.0028660>, 2011.
- 519 Castro-Díez, P., Villar-Salvador, P., Pérez-Rontomé, C., Maestro-Martínez, M., and Montserrat-Martí, G.: Leaf  
520 morphology and leaf chemical composition in three *Quercus* (Fagaceae) species along a rainfall gradient in NE  
521 Spain, *Trees*, 11, 127–134, <https://doi.org/10.1007/PL00009662>, 1997.
- 522 Chen, J. M. and Black, T. A.: Defining leaf area index for non-flat leaves, *Plant Cell Environ.*, 15, 421–429,  
523 <https://doi.org/10.1111/j.1365-3040.1992.tb00992.x>, 1992.
- 524 Coomes, D. A., Holdaway, R. J., Kobe, R. K., Lines, E. R., and Allen, R. B.: A general integrative framework  
525 for modelling woody biomass production and carbon sequestration rates in forests, *Journal of Ecology*, 100, 42–  
526 64, <https://doi.org/10.1111/j.1365-2745.2011.01920.x>, 2012.
- 527 Disney, M.: Terrestrial LiDAR: a three-dimensional revolution in how we look at trees, *New Phytol.*, 222,  
528 1736–1741, <https://doi.org/10.1111/nph.15517>, 2018.
- 529 Flynn, W. R. M., Owen, H. J. F., Grieve, S. W. D., and Lines, E. R.: DHP images collected from Alto Tajo and  
530 Cuellar in Spain. (V1), <https://doi.org/10.5281/ZENODO.7628072>, 2023.
- 531 Gazal, R. M., Scott, R. L., Goodrich, D. C., and Williams, D. G.: Controls on transpiration in a semiarid riparian  
532 cottonwood forest, *Agr. Forest Meteorol.*, 137, 56–67, <https://doi.org/10.1016/j.agrformet.2006.03.002>, 2006.

533 Gower, S. T., Vogel, J. G., Norman, J. M., Kucharik, C. J., Steele, S. J., and Stow, T. K.: Carbon distribution  
534 and aboveground net primary production in aspen, jack pine, and black spruce stands in Saskatchewan and  
535 Manitoba, Canada, *J. Geophys. Res.*, 102, 29029–29041, <https://doi.org/10.1029/97JD02317>, 1997.

536 Gower, S. T., Kucharik, C. J., and Norman, J. M.: Direct and Indirect Estimation of Leaf Area Index, fAPAR,  
537 and Net Primary Production of Terrestrial Ecosystems, *Remote Sens. Environ.*, 70, 29–51,  
538 [https://doi.org/10.1016/S0034-4257\(99\)00056-5](https://doi.org/10.1016/S0034-4257(99)00056-5), 1999.

539 Grotti, M., Calders, K., Origo, N., Puletti, N., Alivernini, A., Ferrara, C., and Chianucci, F.: An intensity, image-  
540 based method to estimate gap fraction, canopy openness and effective leaf area index from phase-shift terrestrial  
541 laser scanning, *Agr. Forest Meteorol.*, 280, 107766, <https://doi.org/10.1016/j.agrformet.2019.107766>, 2020.

542 Hardwick, S. R., Toumi, R., Pfeifer, M., Turner, E. C., Nilus, R., and Ewers, R. M.: The relationship between  
543 leaf area index and microclimate in tropical forest and oil palm plantation: Forest disturbance drives changes in  
544 microclimate, *Agr. Forest Meteorol.*, 201, 187–195, <https://doi.org/10.1016/j.agrformet.2014.11.010>, 2015.

545 Hijmans, R. J.: raster: Geographic Data Analysis and Modeling R package version 3.5-21, [https://CRAN.R-](https://CRAN.R-project.org/package=raster)  
546 [project.org/package=raster.](https://CRAN.R-project.org/package=raster), 2022.

547 Hosoi, F. and Omasa, K.: Voxel-Based 3-D Modeling of Individual Trees for Estimating Leaf Area Density  
548 Using High-Resolution Portable Scanning Lidar, *IEEE T. Geosci. Remote*, 44, 3610–3618,  
549 <https://doi.org/10.1109/TGRS.2006.881743>, 2006.

550 Itakura, K. and Hosoi, F.: Voxel-based leaf area estimation from three-dimensional plant images, *J. Agric.*  
551 *Meteorol.*, 75, 211–216, <https://doi.org/10.2480/agrmet.d-19-00013>, 2019.

552 Jonckheere, I., Fleck, S., Nackaerts, K., Muys, B., Coppin, P., Weiss, M., and Baret, F.: Review of methods for  
553 in situ leaf area index determination, *Agr. Forest Meteorol.*, 121, 19–35,  
554 <https://doi.org/10.1016/j.agrformet.2003.08.027>, 2004.

555 Jonckheere, I. G. C., Muys, B., and Coppin, P.: Allometry and evaluation of in situ optical LAI determination in  
556 Scots pine: a case study in Belgium, *Tree Physiol.*, 25, 723–732, <https://doi.org/10.1093/treephys/25.6.723>,  
557 2005.

558 Jucker, T., Bouriaud, O., Avacaritei, D., Dănilă, I., Duduman, G., Valladares, F., and Coomes, D. A.:  
559 Competition for light and water play contrasting roles in driving diversity-productivity relationships in Iberian  
560 forests, *J. Ecol.*, 102, 1202–1213, <https://doi.org/10.1111/1365-2745.12276>, 2014.

561 Jump, A. S., Ruiz-Benito, P., Greenwood, S., Allen, C. D., Kitzberger, T., Fensham, R., Martínez-Vilalta, J.,  
562 and Lloret, F.: Structural overshoot of tree growth with climate variability and the global spectrum of drought-  
563 induced forest dieback, *Glob. Change Biol.*, 23, 3742–3757, <https://doi.org/10.1111/gcb.13636>, 2017.

564 Jupp, D. L. B., Culvenor, D. S., Lovell, J. L., Newnham, G. J., Strahler, A. H., and Woodcock, C. E.: Estimating  
565 forest LAI profiles and structural parameters using a ground-based laser called 'Echidna(R)', *Tree Physiol.*, 29,  
566 171–181, <https://doi.org/10.1093/treephys/tpn022>, 2008.

567 Kamoske, A. G., Dahlin, K. M., Stark, S. C., and Serbin, S. P.: Leaf area density from airborne LiDAR:  
568 Comparing sensors and resolutions in a temperate broadleaf forest ecosystem, *Forest Ecol. Manag.*, 433, 364–  
569 375, <https://doi.org/10.1016/j.foreco.2018.11.017>, 2019.

570 Kuusk, V., Niinemets, Ü., and Valladares, F.: A major trade-off between structural and photosynthetic  
571 investments operative across plant and needle ages in three Mediterranean pines, *Tree Physiol.*, 38, 543–557,  
572 <https://doi.org/10.1093/treephys/tpx139>, 2018.

573 Leblanc, S. G. and Chen, J. M.: A practical scheme for correcting multiple scattering effects on optical LAI  
574 measurements, *Agr. Forest Meteorol.*, 110, 125–139, [https://doi.org/10.1016/S0168-1923\(01\)00284-2](https://doi.org/10.1016/S0168-1923(01)00284-2), 2001.

575 Lecigne, B., Delagrangé, S., and Messier, C.: Exploring trees in three dimensions: VoxR, a novel voxel-based R  
576 package dedicated to analysing the complex arrangement of tree crowns, *Ann. Bot-London*, 121, 589–601,  
577 <https://doi.org/10.1093/aob/mcx095>, 2018.

- 578 Li, S., Dai, L., Wang, H., Wang, Y., He, Z., and Lin, S.: Estimating Leaf Area Density of Individual Trees  
579 Using the Point Cloud Segmentation of Terrestrial LiDAR Data and a Voxel-Based Model, *Remote Sens-Basel*,  
580 9, 1202, <https://doi.org/10.3390/rs9111202>, 2017.
- 581 Li, Y., Guo, Q., Tao, S., Zheng, G., Zhao, K., Xue, B., and Su, Y.: Derivation, Validation, and Sensitivity  
582 Analysis of Terrestrial Laser Scanning-Based Leaf Area Index, *Can. J. Remote Sens.*, 42, 719–729,  
583 <https://doi.org/10.1080/07038992.2016.1220829>, 2016.
- 584 Lines, E. R., Fischer, F. J., Owen, H. J. F., and Jucker, T.: The shape of trees: Reimagining forest ecology in  
585 three dimensions with remote sensing, *J. Ecol.*, 110, 1730–1745, <https://doi.org/10.1111/1365-2745.13944>,  
586 2022.
- 587 Long, J. N. and Smith, F. W.: Leaf area - sapwood area relations of lodgepole pine as influenced by stand  
588 density and site index., *Can. J. Forest Res.*, 18, 247–250, 1988.
- 589 López, R., Cano, F. J., Martin-StPaul, N. K., Cochard, H., and Choat, B.: Coordination of stem and leaf traits  
590 define different strategies to regulate water loss and tolerance ranges to aridity, *New Phytol.*, 230, 497–509,  
591 <https://doi.org/10.1111/nph.17185>, 2021.
- 592 Lovell, J. L., Jupp, D. L. B., van Gorsel, E., Jimenez-Berni, J., Hopkinson, C., and Chasmer, L.: Foliage Profiles  
593 from Ground Based Waveform and Discrete Point Lidar, *SilviLaser*, 1–9, 2011.
- 594 Ma, L., Zheng, G., Eitel, J. U. H., Magney, T. S., and Moskal, L. M.: Determining woody-to-total area ratio  
595 using terrestrial laser scanning (TLS), *Agr. Forest Meteorol.*, 228–229, 217–228,  
596 <https://doi.org/10.1016/j.agrformet.2016.06.021>, 2016.
- 597 Madrigal-González, J., Herrero, A., Ruiz-Benito, P., and Zavala, M. A.: Resilience to drought in a dry forest:  
598 Insights from demographic rates, *Forest Ecol. Manag.*, 389, 167–175,  
599 <https://doi.org/10.1016/j.foreco.2016.12.012>, 2017.
- 600 Magnani, F., Mencuccini, M., and Grace, J.: Age-related decline in stand productivity: the role of structural  
601 acclimation under hydraulic constraints, *Plant Cell Environ.*, 23, 251–263, <https://doi.org/10.1046/j.1365-3040.2000.00537.x>, 2000.
- 603 Mencuccini, M.: The ecological significance of long-distance water transport: short-term regulation, long-term  
604 acclimation and the hydraulic costs of stature across plant life forms, *Plant Cell Environ.*, 26, 163–182,  
605 <https://doi.org/10.1046/j.1365-3040.2003.00991.x>, 2003.
- 606 Mencuccini, M. and Grace, J.: Climate influences the leaf area/sapwood area ratio in Scots pine, *Tree Physiol.*,  
607 15, 1–10, <https://doi.org/10.1093/treephys/15.1.1>, 1995.
- 608 Monsi, M. and Saeki, T.: On the Factor Light in Plant Communities and its Importance for Matter Production,  
609 *Ann. Bot-London*, 95, 549–567, <https://doi.org/10.1093/aob/mci052>, 1953.
- 610 Nakagawa, S., Johnson, P. C. D., and Schielzeth, H.: The coefficient of determination R<sup>2</sup> and intra-class  
611 correlation coefficient from generalized linear mixed-effects models revisited and expanded, *J. R. Soc.*  
612 *Interface*, 14, 20170213, <https://doi.org/10.1098/rsif.2017.0213>, 2017.
- 613 Niinemets, Ü. and Valladares, F.: Tolerance to shade, drought, and waterlogging of temperate northern  
614 hemisphere trees and shrubs, *Ecol. Monogr.*, 76, 521–547, [https://doi.org/10.1890/0012-9615\(2006\)076\[0521:TTSDAW\]2.0.CO;2](https://doi.org/10.1890/0012-9615(2006)076[0521:TTSDAW]2.0.CO;2), 2006.
- 616 Niu, X., Fan, J., Luo, R., Fu, W., Yuan, H., and Du, M.: Continuous estimation of leaf area index and the  
617 woody-to-total area ratio of two deciduous shrub canopies using fisheye webcams in a semiarid loessial region  
618 of China, *Ecol. Indic.*, 125, 107549, <https://doi.org/10.1016/j.ecolind.2021.107549>, 2021.
- 619 Olivas, P. C., Oberbauer, S. F., Clark, D. B., Clark, D. A., Ryan, M. G., O'Brien, J. J., and Ordoñez, H.:  
620 Comparison of direct and indirect methods for assessing leaf area index across a tropical rain forest landscape,  
621 *Agr. Forest Meteorol.*, 177, 110–116, <https://doi.org/10.1016/j.agrformet.2013.04.010>, 2013.

- 622 Owen, H. J. F., Flynn, W. R. M., and Lines, E. R.: Competitive drivers of inter-specific deviations of crown  
623 morphology from theoretical predictions measured with Terrestrial Laser Scanning, *J. Ecol.*, 109, 2612–2628,  
624 <https://doi.org/10.1111/1365-2745.13670>, 2021.
- 625 Owen, H. J. F., Flynn, W. R. M., and Lines, E. R.: Individual TLS tree clouds collected from both Alto Tajo and  
626 Cuellar in Spain., 2022.
- 627 Peppe, D. J., Royer, D. L., Cariglino, B., Oliver, S. Y., Newman, S., Leight, E., Enikolopov, G., Fernandez-  
628 Burgos, M., Herrera, F., Adams, J. M., Correa, E., Currano, E. D., Erickson, J. M., Hinojosa, L. F., Hoganson, J.  
629 W., Iglesias, A., Jaramillo, C. A., Johnson, K. R., Jordan, G. J., Kraft, N. J. B., Lovelock, E. C., Lusk, C. H.,  
630 Niinemets, Ü., Peñuelas, J., Rapson, G., Wing, S. L., and Wright, I. J.: Sensitivity of leaf size and shape to  
631 climate: global patterns and paleoclimatic applications, *New Phytol.*, 190, 724–739,  
632 <https://doi.org/10.1111/j.1469-8137.2010.03615.x>, 2011.
- 633 Pfeifer, M., Gonsamo, A., Disney, M., Pellikka, P., and Marchant, R.: Leaf area index for biomes of the Eastern  
634 Arc Mountains: Landsat and SPOT observations along precipitation and altitude gradients, *Remote Sens.*  
635 *Environ.*, 118, 103–115, <https://doi.org/10.1016/j.rse.2011.11.009>, 2012.
- 636 Phillips, N., Bond, B. J., McDowell, N. G., Ryan, M. G., and Schauer, A.: Leaf area compounds height-related  
637 hydraulic costs of water transport in Oregon White Oak trees, *Funct. Ecol.*, 17, 832–840,  
638 <https://doi.org/10.1111/j.1365-2435.2003.00791.x>, 2003.
- 639 Purves, D. and Pacala, S.: Predictive Models of Forest Dynamics, *Science*, 320, 1452–1453,  
640 <https://doi.org/10.1126/science.1155359>, 2008.
- 641 Ridler, T. W. and Calvard, S.: Picture Thresholding Using an Iterative Selection Method, *IEEE T. Syst. Man.*  
642 *Cyb.*, 8, 630–632, <https://doi.org/10.1109/TSMC.1978.4310039>, 1978.
- 643 Sea, W. B., Choler, P., Beringer, J., Weinmann, R. A., Hutley, L. B., and Leuning, R.: Documenting  
644 improvement in leaf area index estimates from MODIS using hemispherical photos for Australian savannas,  
645 *Agr. Forest Meterol.*, 151, 1453–1461, <https://doi.org/10.1016/j.agrformet.2010.12.006>, 2011.
- 646 Specht, R. L. and Specht, A.: Canopy structure in Eucalyptus-dominated communities in Australia along  
647 climatic gradients, *Canopy structure in Eucalyptus-dominated communities in Australia along climatic*  
648 *gradients*, 10, 191–213, 1989.
- 649 Vicari, M. B., Disney, M., Wilkes, P., Burt, A., Calders, K., and Woodgate, W.: Leaf and wood classification  
650 framework for terrestrial LiDAR point clouds, *Methods Ecol. Evol.*, 10, 680–694, [https://doi.org/10.1111/2041-](https://doi.org/10.1111/2041-210X.13144)  
651 [210X.13144](https://doi.org/10.1111/2041-210X.13144), 2019.
- 652 Warton, D. I., Wright, I. J., Falster, D. S., and Westoby, M.: Bivariate line-fitting methods for allometry, *Biol.*  
653 *Rev.*, 81, 259–291, <https://doi.org/10.1017/S1464793106007007>, 2006.
- 654 Warton, D. I., Duursma, R. A., Falster, D. S., and Taskinen, S.: smatr 3 - an R package for estimation and  
655 inference about allometric lines: *The smatr 3 - an R package*, *Methods Ecol. Evol.*, 3, 257–259,  
656 <https://doi.org/10.1111/j.2041-210X.2011.00153.x>, 2012.
- 657 Weiss, M., Baret, F., Smith, G. J., Jonckheere, I., and Coppin, P.: Review of methods for in situ leaf area index  
658 (LAI) determination, *Agr. Forest Meterol.*, 121, 37–53, <https://doi.org/10.1016/j.agrformet.2003.08.001>, 2004.
- 659 Whitehead, D.: The Estimation of Foliage Area from Sapwood Basal Area in Scots Pine, *Forestry*, 51, 137–149,  
660 <https://doi.org/10.1093/forestry/51.2.137>, 1978.
- 661 Wilkes, P., Lau, A., Disney, M., Calders, K., Burt, A., Gonzalez de Tanago, J., Bartholomeus, H., Brede, B., and  
662 Herold, M.: Data acquisition considerations for Terrestrial Laser Scanning of forest plots, *Remote Sensing of*  
663 *Environment*, 196, 140–153, <https://doi.org/10.1016/j.rse.2017.04.030>, 2017.
- 664 Woodgate, W., Jones, S. D., Suarez, L., Hill, M. J., Armston, J. D., Wilkes, P., Soto-Berelov, M., Haywood, A.,  
665 and Mellor, A.: Understanding the variability in ground-based methods for retrieving canopy openness, gap

- 666 fraction, and leaf area index in diverse forest systems, *Agr. Forest Meteorol.*, 205, 83–95,  
667 <https://doi.org/10.1016/j.agrformet.2015.02.012>, 2015.
- 668 Woodgate, W., Armston, J. D., Disney, M., Jones, S. D., Suarez, L., Hill, M. J., Wilkes, P., and Soto-Berelev,  
669 M.: Quantifying the impact of woody material on leaf area index estimation from hemispherical photography  
670 using 3D canopy simulations, *Agr. Forest Meteorol.*, 226–227, 1–12,  
671 <https://doi.org/10.1016/j.agrformet.2016.05.009>, 2016.
- 672 Zhang, Y., Chen, J. M., and Miller, J. R.: Determining digital hemispherical photograph exposure for leaf area  
673 index estimation, *Agr. Forest Meteorol.*, 133, 166–181, <https://doi.org/10.1016/j.agrformet.2005.09.009>, 2005.
- 674 Zheng, G., Moskal, L. M., and Kim, S.-H.: Retrieval of Effective Leaf Area Index in Heterogeneous Forests  
675 With Terrestrial Laser Scanning, *IEEE T. Geosci. Remote*, 51, 777–786,  
676 <https://doi.org/10.1109/TGRS.2012.2205003>, 2013.
- 677 Zhu, X., Skidmore, A. K., Wang, T., Liu, J., Darvishzadeh, R., Shi, Y., Premier, J., and Heurich, M.: Improving  
678 leaf area index (LAI) estimation by correcting for clumping and woody effects using terrestrial laser scanning,  
679 *Agr. Forest Meteorol.*, 263, 276–286, <https://doi.org/10.1016/j.agrformet.2018.08.026>, 2018.
- 680